

Article

Synthesis of Cobalt-Based Nanoparticles as Catalysts for Methanol Synthesis from CO₂ Hydrogenation

Anna Carrasco-García ¹, Seyed Alireza Vali ¹, Zahra Ben-Abbou ¹, Javier Moral-Vico ¹, Ahmad Abo Markeb ^{1,2}
and Antoni Sánchez ^{1,*}

¹ Department of Chemical, Biological and Environmental Engineering, Escola d'Enginyeria, Universitat Autònoma de Barcelona, 08193 Cerdanyola del Vallès, Spain

² Department of Chemistry, Faculty of Science, Assiut University, Assiut 71516, Egypt

* Correspondence: antoni.sanchez@uab.cat

Abstract: The increasing emission of carbon dioxide into the atmosphere has urged the scientific community to investigate alternatives to alleviate such emissions, being that they are the principal contributor to the greenhouse gas effect. One major alternative is carbon capture and utilization (CCU) toward the production of value-added chemicals using diverse technologies. This work aims at the study of the catalytic potential of different cobalt-derived nanoparticles for methanol synthesis from carbon dioxide hydrogenation. Thanks to its abundance and cost efficacy, cobalt can serve as an economical catalyst compared to noble metal-based catalysts. In this work, we present a systematic comparison among different cobalt and cobalt oxide nanocomposites in terms of their efficiency as catalysts for carbon dioxide hydrogenation to methanol as well as how different supports, zeolites, MnO₂, and CeO₂, can enhance their catalytic capacity. The oxygen vacancies in the cerium oxide act as carbon dioxide adsorption and activation sites, which facilitates a higher methanol production yield.

Keywords: carbon dioxide hydrogenation; methanol synthesis; nanomaterials; heterogeneous catalysis; metal–support interaction



Citation: Carrasco-García, A.; Vali, S.A.; Ben-Abbou, Z.; Moral-Vico, J.; Abo Markeb, A.; Sánchez, A. Synthesis of Cobalt-Based Nanoparticles as Catalysts for Methanol Synthesis from CO₂ Hydrogenation. *Materials* **2024**, *17*, 697. <https://doi.org/10.3390/ma17030697>

Academic Editors: Raphaël Schneider and Carlos Javier Duran-Valle

Received: 30 October 2023

Revised: 22 January 2024

Accepted: 28 January 2024

Published: 1 February 2024



Copyright: © 2024 by the authors. Licensee MDPI, Basel, Switzerland. This article is an open access article distributed under the terms and conditions of the Creative Commons Attribution (CC BY) license (<https://creativecommons.org/licenses/by/4.0/>).

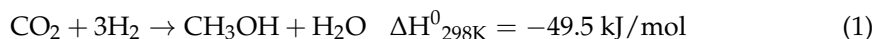
1. Introduction

Nowadays, one of the main worldwide concerns is the slow but unstoppable rise in global average temperature, a direct cause of climate change that seems almost unavoidable. The high quantities of greenhouse gases emitted into the atmosphere, of which carbon dioxide emissions are the most important, predict an increase in the Earth's temperature by 2040 of approximately 1.5 °C compared to the data recorded at the end of the 19th century [1]. Such predictions have alerted the scientific community to develop protocols to lower carbon dioxide emissions, which can be classified according to whether they are carbon capture and storage (CCS) or carbon capture and utilization (CCU) methods. On one hand, CCS methods consist of capturing and storing the gas, and it is so efficient that it could account for almost 20% of the carbon dioxide reduction. Nevertheless, it can be quite costly because industrial-scale installations have to be built. Unfortunately, fossil fuels are still needed as an energy source for this treatment, so carbon dioxide reduction will never be fully completed [2].

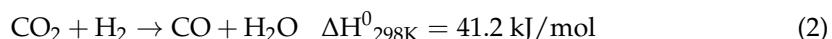
On the other hand, CCU results are remarkably interesting since CCU does not only deal with the storage of carbon dioxide but it takes advantage of this gas as a valuable carbon resource for chemical conversion into other products. This is a more viable strategy, as it could not only keep the atmospheric concentration of CO₂ at acceptable levels but also provide high added-value chemical/fuel products, such as methane and methanol [3,4]. Among all the technologies, carbon dioxide hydrogenation has been considered a promising alternative for obtaining some products from carbon dioxide. An attractive possibility is the production of methanol, a chemical compound that has a wide range of applications.

For instance, it can be used as a solvent to obtain several chemicals (formaldehyde, acetic acid, etc.), as well as in the conversion process to olefins, which can be used to produce hydrocarbon fuels and their derivatives that are currently obtained from petroleum [5,6].

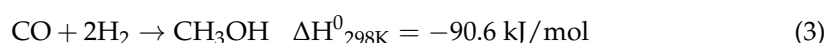
Carbon dioxide hydrogenation to methanol occurs through two competing reactions. The first step is the methanol synthesis from carbon dioxide and hydrogen:



The second step is known as the reverse water–gas shift reaction (RWGS), leading to carbon monoxide production:



In addition, methanol can be indirectly produced from carbon monoxide hydrogenation via the RWGS reaction [7]:



The synthesis of methanol is thermodynamically favored at low temperatures and high pressures [8,9].

In recent years, bimetallic catalysts have been elaborately studied owing to their chemical, electronic, and structural characteristics. Additionally, the synergy between metals leads to the generation of a catalytic system, which, unlike monometallic systems, presents advantages in terms of catalytic activity, methanol selectivity, and catalyst stability [10]. The catalysts for carbon dioxide hydrogenation to methanol studied more comprehensively include Cu-Zn-based catalysts, although other bimetallic catalysts such as Pd-Zn, Pd-Ga, Cu-Ni, and Ni-Ga have been investigated as well [7]. In addition to these mentioned catalysts, methanol has also been obtained using cobalt-based catalysts. Stangeland et al. [11] demonstrated that $\text{Co}_3\text{O}_4/\text{MnO}_x$ was efficient in the production of methanol at mild pressures, but a variety of by-products were also obtained. These authors achieved a manifold increase in methanol yield with $\text{Co}_3\text{O}_4/\text{MnO}_x$ catalysts compared to Cu/Zn-based catalysts under similar reaction conditions [11]. Wang et al. [12] investigated silica-supported cobalt catalysts with the aim of accelerating the selectivity of methanol obtained from the carbon dioxide hydrogenation, and they showed that silica incorporation in the cobalt catalysts improved both carbon dioxide conversion and selectivity toward methanol.

One of the significant features of cobalt-based catalysts is their potential to catalyze various carbon dioxide conversion reactions such as methanation [13,14], synthesis of higher alcohols [15,16], or methanol synthesis [11,12,17,18]. In these investigations, it was shown that the selectivity of these catalysts can be impacted by the use of different supports. In the present study, different supports including zeolite, manganese oxide, and cerium oxide have been investigated to increase the catalytic activity of cobalt-based catalysts. It is hypothesized that different metal–support interactions between cobalt nanoparticles and the support will enhance the catalytic sites, leading to higher methanol yield and selectivity. Zeolites with a microporous three-dimensional structure based on SiO_4 and AlO_4 present substantial catalytic and adsorption properties [19]. Cerium oxide is a non-toxic oxide, which is of great importance in catalysis due to its ability to store and supply oxygen [20,21]. It provides a large number of oxygen vacancies on the surface, which can function as sites for the adsorption and activation of carbon dioxide. Manganese oxide is a mesoporous support and its effect as support for nanocatalysts used for carbon dioxide hydrogenation to methanol has not been reported [11].

Capping agents are reported to be significant stabilizers since they counteract the attraction between nanoparticles, thus inhibiting their overgrowth and aggregation. These agents are amphiphathic molecules that are characterized by having a polar head group and a non-polar tail, and due to this amphiphathic property, they improve compatibility with other phases. Different types of protection agents have been implemented in the synthesis of

nanomaterials (surfactants, polymers, polysaccharides, etc.), aiming to obtain nanoparticles of smaller sizes, which will lead to the highest surface area of nanoparticles [22,23]. In this study, the agglomeration of the synthesized nanoparticles was controlled by steric stabilization using polyvinylpyrrolidone (PVP).

This work is centered on studying the catalytic activity of supported and unsupported cobalt-based nanoparticles. The aim is to evaluate this type of nanomaterial in order to obtain high methanol production yields and high selectivity under mild pressure and temperature conditions.

2. Materials and Methods

2.1. Materials

Sodium borohydride (NaBH_4) (99.0%), cobalt (II) chloride hexahydrate ($\text{CoCl}_2 \cdot 6\text{H}_2\text{O}$) (99.0%), polyvinylpyrrolidone (PVP), sodium carbonate (Na_2CO_3) (99.5%), zeolite, cerium (III) nitrate hexahydrate ($\text{Ce}(\text{NO}_3)_3 \cdot 6\text{H}_2\text{O}$) (99.0%), sodium hydroxide (NaOH) (98.0%), manganese (II) sulfate monohydrate ($\text{MnSO}_4 \cdot \text{H}_2\text{O}$) (99.0%), and potassium permanganate (KMnO_4) (99.5%) were all purchased from Sigma-Aldrich (Barcelona, Spain). A mixed-gas bottle of carbon dioxide and hydrogen with a molar ratio of 1:3, respectively, was provided by Carburos Metálicos S.A. (Barcelona, Spain).

2.2. Synthesis of Nanocomposites

2.2.1. Co nanoparticles Synthesis

Co nanoparticles were synthesized by the chemical reduction method. A total of 1.10 g of cobalt (II) chloride hexahydrate was dissolved in 100 mL of deionized water with magnetic stirring and nitrogen bubbling to avoid the oxidation of cobalt. Then, a solution of sodium borohydride (0.25 M) was added dropwise, and the solution was left to stir for 20 min to ensure all the cobalt was reduced [24]. Once the reaction was complete, the pH reached 9.3, and cobalt nanoparticles were separated using a magnet. The product was washed three times with deionized water to remove any impurities and dried in an oven at 105 °C overnight. Co nanoparticles with PVP were synthesized via a similar route by adding 1.10 g of PVP to the cobalt (II) chloride hexahydrate solution.

2.2.2. Co_3O_4 Nanoparticles Synthesis

Co_3O_4 nanoparticles were synthesized via the co-precipitation method. Briefly, 0.61 g of cobalt (II) chloride hexahydrate was dissolved in 100 mL of deionized water using magnetic stirring for 20 min. The synthesis was performed in a 500 mL Scharlau Minireactor HME-R/500 with mechanical stirring and heating at constant ambient pressure. Cobalt (II) chloride hexahydrate solution was added to the reactor and the precipitation agent, sodium carbonate solution (1 M), was added dropwise at a flow rate of 5 mL/min using a peristaltic pump (Watson Marlow SCI 400, Watson-Marlow GmbH, Rommerskirchen, Germany), and the solution was left to age at 60 °C for 5 h with constant stirring at 120 rpm. The Co_3O_4 nanoparticles were obtained after centrifuging three times for 15 min at 5000 rpm and drying at 105 °C overnight [24]. Co_3O_4 nanoparticles with PVP were synthesized via a similar route by adding 0.62 g PVP to the cobalt (II) chloride hexahydrate solution.

2.2.3. MnO_2 Nanoparticles Synthesis

The co-precipitation method was also employed for the synthesis of MnO_2 nanoparticles. A total of 3.12 g of manganese (II) sulfate monohydrate was dissolved in 100 mL deionized water. The potassium permanganate solution (0.15 M) was added to the above solution dropwise, and the mixture was vigorously stirred in a Scharlau Minireactor HME-R/500 (Barcelona, Spain) at 80 °C for 5 h. Then, a sodium hydroxide solution was added dropwise to adjust the pH to 11. Afterwards, the nanoparticles were centrifuged and washed three times with deionized water. Finally, the nanoparticles obtained were dried at 105 °C for 12 h [25].

2.2.4. Co₃O₄/Zeolite Nanocomposite Synthesis

To immobilize the Co₃O₄ nanoparticles onto zeolite, the same Co₃O₄ synthesis described above was followed. In 200 mL of ultrapure water, 1 g of zeolite was dispersed in an ultrasound bath for 15 min. Once zeolite was dispersed, it was transferred to the reactor, and the same Co₃O₄ synthesis procedure was performed.

2.2.5. CeO₂ Nanoparticle Synthesis

CeO₂ nanoparticles were synthesized through a co-precipitation method as well. A total of 5.12 g of cerium (III) nitrate hexahydrate was dissolved in another 100 mL of deionized water. Then, 1.88 g of the precipitant agent, sodium hydroxide, was dissolved in 100 mL of deionized water and was added dropwise to cerium solution in a reactor (Scharlau Minireactor HME-R/500, Scharlab, Barcelona, Spain) with mechanical agitation using a peristaltic pump at 7 mL/min. The solution was then left for 15 min under stirring. Eventually, the precipitates obtained were centrifuged, washed with deionized water three times, and then dried at 105 °C overnight [26].

2.2.6. Co₃O₄/CeO₂ Nanocomposite Synthesis

To immobilize the Co₃O₄ nanoparticles onto CeO₂, the same Co₃O₄ synthesis procedure was followed. In 200 mL of deionized water, the nanoparticles of CeO₂ were scattered in an ultrasound bath for 15 min. Once dispersed, the same Co₃O₄ synthesis procedure was carried out, but first, the solution of the CeO₂ nanoparticles was transferred to the reactor. The resulting weight ratio of Co₃O₄ nanoparticles and CeO₂ supports was 2:1 (g/g), respectively.

2.2.7. Co₃O₄/MnO₂ Nanocomposite Synthesis

Co₃O₄ nanocomposites were synthesized using the co-precipitation method. The same Co₃O₄ synthesis procedure followed, but first, the previously synthesized MnO₂ nanoparticles were dispersed in 200 mL of deionized water in an ultrasound bath for 15 min. Subsequently, the same Co₃O₄ synthesis was followed after MnO₂ was added to the reactor. The resulting weight ratio of Co₃O₄ nanoparticles and MnO₂ supports was 2:1 (g/g), respectively.

2.3. Characterization of Catalysts

X-ray diffraction (XRD) was used to perform a structural analysis of the nanoparticles and their crystallographic structure. All the analyses were conducted after the materials had been thermally treated. A diffractometer (PANalytical X'Pert, Malvern Panalytical, Malvern, UK) using Cu-K α radiation was employed to record the X-ray diffraction patterns. The measurements were conducted at room temperature in a range of 10.0–80.0° on 2 θ with a step size of 0.026°. The data analysis was completed by simulating the nanoparticles' crystallinity with the X'Pert High Score (PANalytical) software (Version 3.0.5). A scanning electron microscope (SEM) (FEI Quanta 650F ESEM, FEI, Hillsboro, OR, USA) equipped with an energy-dispersive spectroscopy (EDS) source was used to determine the morphology, size distribution, and composition of the nanoparticles. Samples were prepared on copper and graphite grids (TED PELLA, Inc., Redding, CA, USA). The microstructure, the size, morphology, and size distribution of the nanoparticles were determined using a transmission electron microscope (TEM) (FEI TECNAI G2 F20, FEI, Hillsboro, OR, USA). The samples were analyzed using copper grids (TED PELLA, Inc., Redding, CA, USA). An AutoChem (Micromeritics) instrument using 12 vol% H₂/Ar at a flow of 50 N mL·min⁻¹ in a temperature range of 35–800 °C at a heating ramp of 10 °C·min⁻¹ was used for temperature-programmed reduction (H₂-TPR) measurements. The amount of H₂ uptake was measured with a thermal conductivity detector. A total of 100 mg of the sample was used for each measurement.

2.4. Catalytic Activity Test

The catalytic test was carried out in a stainless-steel fixed-bed reactor. Prior to the tests, samples were calcinated at 500 °C for 4 h, and those containing elemental cobalt were reduced by a hydrogen flow of 40 mL/min at 350 °C for 2 h. The catalyst samples were fixed between two layers of glass wool at each end of the reactor. The catalytic tests were carried out under two moderate pressure values of 10 and 15 bar. The flow rate of the stoichiometric H₂/CO₂ mixture was 10 mL/min. To study the impact of reaction temperature on the catalytic activity, the reaction was performed at temperatures ranging from 180 to 280 °C. After fixing each temperature, catalysts were stabilized for half an hour, resulting in a total time of operation of more than four hours. Sampling bags (SKC FlexFoil PLUS Sample Bag, SKC, Seoul, Republic of Korea) were utilized to collect the gas samples, and methanol was measured in a gas chromatograph (Shimadzu GC-2010, Shimadzu, Kyoto, Japan) with a flame ionization detector (FID) using helium as carrier gas. The software used was Chromeleon (Version 6.80 SR5b), the inlet temperature was 260 °C, and the flow was 50 mL/min; the detector temperature was 280 °C. An Agilent 7890B chromatograph (Agilent, Santa Clara, CA, USA) was used to measure carbon monoxide and dioxide, employing a thermal conductivity detector (TCD) and helium as the carrier gas. The software used was OpenLab (Version A.01.04), the inlet temperature was 120 °C, the inlet flow was 20 mL/min, and the detector temperature was 150 °C. To study the catalytic activity, methanol space–time yield (STY), as well as methanol selectivity, were calculated according to the following equations. Carbon monoxide was observed to be the only side-product of the reaction.

$$\text{CH}_3\text{OH STY} \left(\frac{\text{g}}{\text{kg}_{\text{cat}} \times \text{h}} \right) = \left(\frac{\text{Mass of methanol (g) formed}}{W_{\text{cat}}(\text{kg}) \times \text{Hour}} \right) \quad (4)$$

$$\text{CH}_3\text{OH Selectivity}(\%) = \left(\frac{\text{moles of methanol formed}}{n[\text{CO}_2]_{\text{in}} - n[\text{CO}_2]_{\text{out}}} \right) \times 100 \quad (5)$$

3. Results and Discussion

3.1. Structural and Morphological Characterization of Nanomaterials

The XRD patterns obtained for cobalt and cobalt oxide with and without capping agents (PVP) and their corresponding simulations using PANALYTICAL X'Pert High Score software are presented in Figure 1. As is shown, the peaks at diffraction angles of 2θ of 19.05°, 31.27°, 36.90°, 38.56°, 44.82°, 55.70°, 59.40°, 65.30°, 74.14°, and 77.14° correspond to the (111), (220), (311), (222), (400), (422), (511), (440), (620), and (533) planes of Co₃O₄ [11,23,27]. Furthermore, the peaks at 2θ of 44.23° (111) and 51.52° (200) corresponded to Co nanoparticles [24]. It can also be observed that the XRD spectra of the synthesized materials are very similar to the simulation, which means a high level of purity and crystallinity. Regarding the Co₃O₄ and Co with and without PVP, it was observed that PVP did not interfere with the crystallinity of cobalt and cobalt oxide nanoparticles. As can be seen, there is no presence of cobalt oxide in the cobalt XRD patterns, indicating that the synthesis of cobalt nanoparticles was satisfactory, and all the nanoparticles were completely reduced.

The X-ray diffraction patterns of all the supports are shown in Figure 2. Regarding two of the supports, CeO₂ and MnO₂, it is observed that not all the peaks observed in the simulation correspond to the peaks observed in the synthesized sample, which indicates that these samples are not completely crystalline. However, the peaks obtained for the zeolite sample show a more crystalline structure, with a spectrum that is more similar to the simulation than in the case of the other two supports.

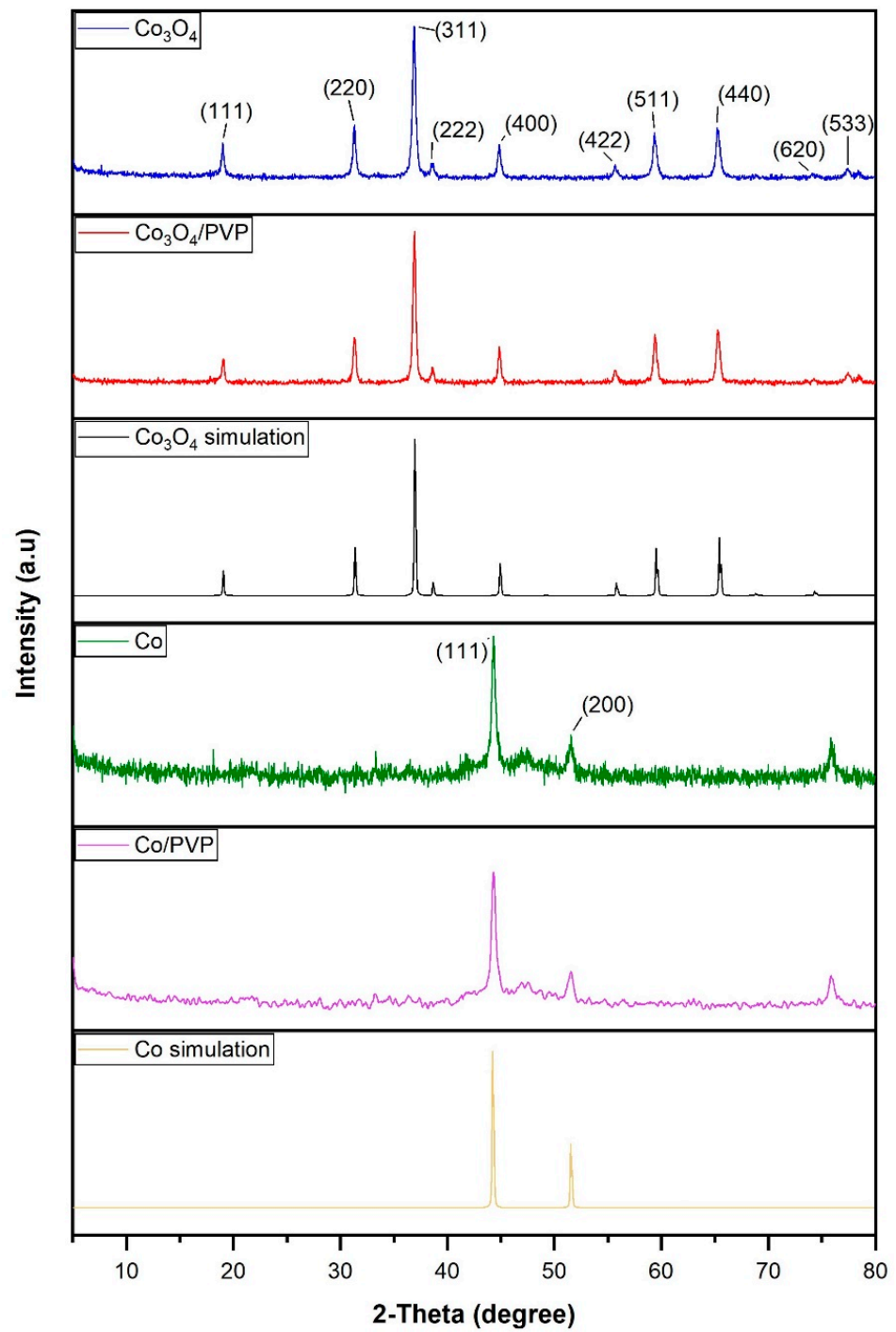


Figure 1. XRD patterns of the following samples and simulations: Co simulation; Co nanoparticles; Co/PVP nanoparticles; Co₃O₄ nanoparticles; Co₃O₄/PVP nanoparticles; Co₃O₄ simulation.

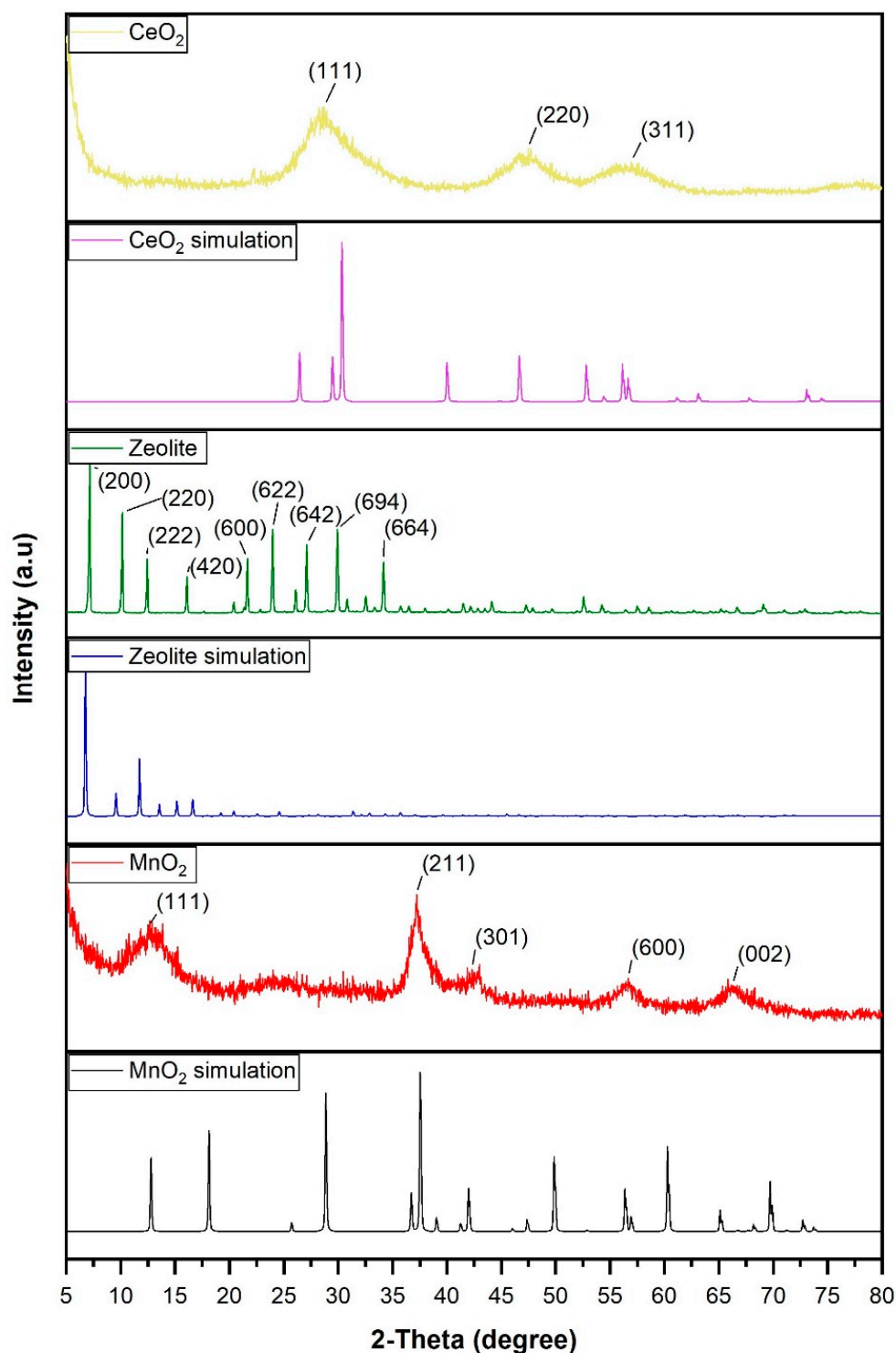


Figure 2. XRD patterns of the following samples and simulations: CeO_2 ; CeO_2 simulation; zeolite; zeolite simulation; MnO_2 ; MnO_2 simulation.

The X-ray diffraction patterns of the nanoparticles and their supports are shown in Figure 3. Regarding the highest peaks of Co_3O_4 /zeolite, it is observed that the first peaks are associated with zeolite since the X'Pert High Score software determined that they correspond to the two typical elements of zeolite (aluminum and silicon) [28]. Small peaks corresponding to Co_3O_4 were also observed at the following angles: 19.05° , 31.27° , 36.90° , 38.56° , 44.82° , 55.70° , 59.40° , and 65.30° . Regarding the XRD patterns of Co_3O_4 / CeO_2 , it is

observed that the peaks situated at the angles of 28.50° , 33.10° , 47.50° , 56.30° , 69.40° , 76.70° , and 79.10° belong to CeO_2 . They are associated with planes (111), (200), (220), (311), (400), (331), and (420), respectively (Figure 3) [27]. Moreover, other characteristic peaks of Co_3O_4 are seen at angles 19.05° , 31.27° , 36.90° , 38.56° , 44.82° , 59.4° , and 65.30° (Figure 3) [29,30]. Finally, in the $\text{Co}_3\text{O}_4/\text{MnO}_2$ patterns, the peaks of both materials can also be visualized (Figure 3). The angles 24.50° , 41.60° , 50.30° , 54.70° , 63.70° , 72.30° , and 79.19° correspond to $\text{Co}_3\text{O}_4/\text{MnO}_2$ and are related to the (110), (120), (220), (231), (130), (343), and (330) planes (Figure 3) [31,32]. Another wide peak around 58° is probably the peak at 59.4° attributed to Co_3O_4 , which is broadened due to the interaction with MnO_2 . The other profiles observed correspond to the cobalt oxides present in the sample since they coincide with the Co_3O_4 angles described above. This means that there is a coexistence of elemental cobalt and its oxidized species in the sample.

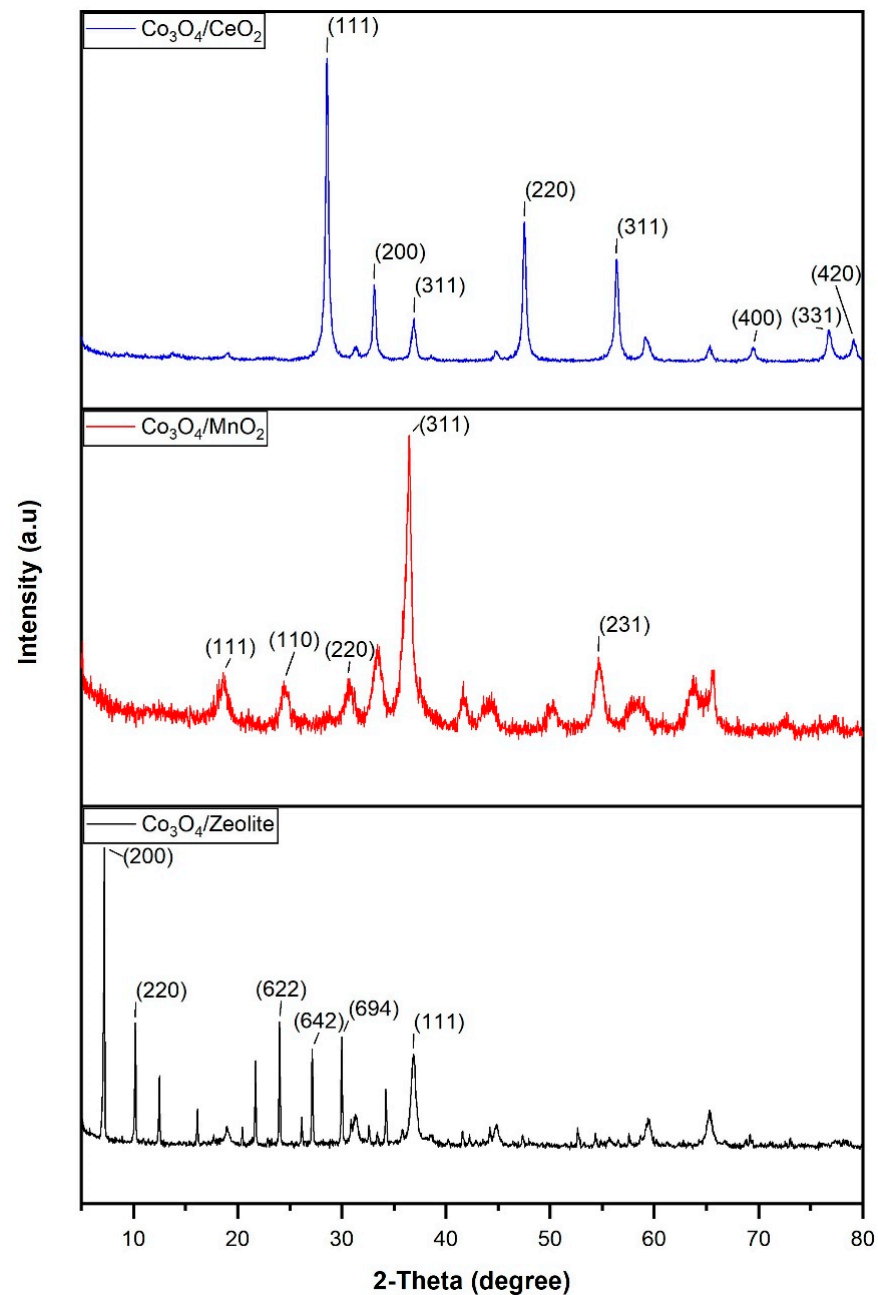


Figure 3. XRD patterns of the following samples: $\text{Co}_3\text{O}_4/\text{CeO}_2$; $\text{Co}_3\text{O}_4/\text{MnO}_2$; $\text{Co}_3\text{O}_4/\text{zeolite}$.

The characterization and morphology study of the materials was performed using a scanning electron microscope (SEM) and a transmission electron microscope (TEM). Figure 4C shows the SEM image of the Co_3O_4 nanoparticles, which presents an irregular shape with a high degree of agglomeration, as previously reported [24]. Nevertheless, when PVP was added, the nanoparticles were smaller and with a more spherical geometry (Figure 4D). The nanoparticle sizes were determined by analyzing TEM images with ImageJ software (Version 1.46r) (Figure 5). The mean size for Co_3O_4 nanoparticles was 27 ± 5 nm (Figure 5B), whereas when PVP was used, the size was reduced to 15 ± 2.5 nm (Figure 5B,E), confirming the observation of SEM images. It is reported in the literature that by adding a capping agent, the nanoparticles are smaller, and this effect leads to an increase in the surface area of the catalyst, which means that the active sites are more exposed [22,23]. Therefore, the catalytic activity of the catalyst increases. The morphology of cobalt nanoparticles with and without PVP is shown in Figure 4A,B, respectively. The same effect is observed when PVP was added to the synthesized material: the morphology obtained is well defined and the particles are smaller.

SEM images of nanoparticles embedded in a support are presented in Figure 6. Co_3O_4 nanoparticles immobilized on zeolite show a granular morphology (Figure 6A). The TEM image of the same sample shows a good dispersion of cobalt oxide nanoparticles, and a mean size of 13 ± 1.7 nm (Figure 5D), which means that these cobalt oxide nanoparticles are even smaller than those synthesized in the presence of PVP. It is reported in the literature that the use of a support helps to obtain nanoparticles with better distribution and a higher surface area [30]. In Figure 6C, Co_3O_4 nanoparticles supported on CeO_2 can be observed, demonstrating that the nanoparticles have a very small size and a good distribution. Indeed, the Co_3O_4 nanoparticles supported on CeO_2 analyzed with TEM (Figure 5C) reveal a size of 22.6 ± 4.2 nm for the former, which is slightly smaller than unsupported Co_3O_4 (27 ± 5 nm). Figure 5C also shows a good interaction between cobalt and cerium oxide nanoparticles.

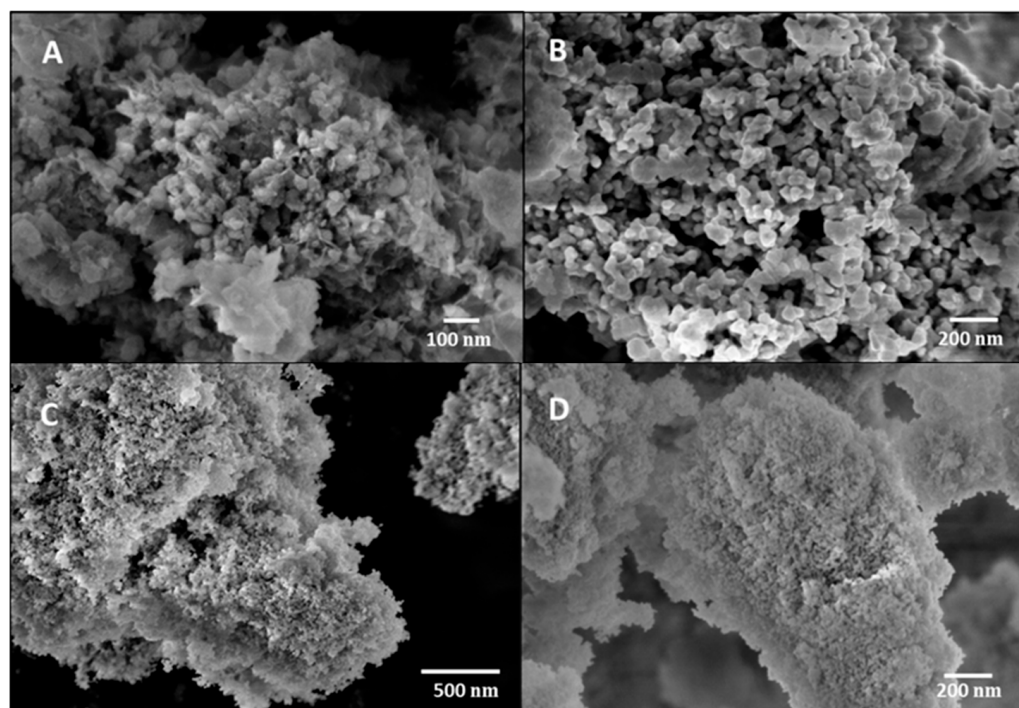


Figure 4. SEM images obtained from the catalyst samples: (A) Co nanoparticles; (B) Co/PVP nanoparticles; (C) Co_3O_4 nanoparticles; (D) Co_3O_4 /PVP nanoparticles.

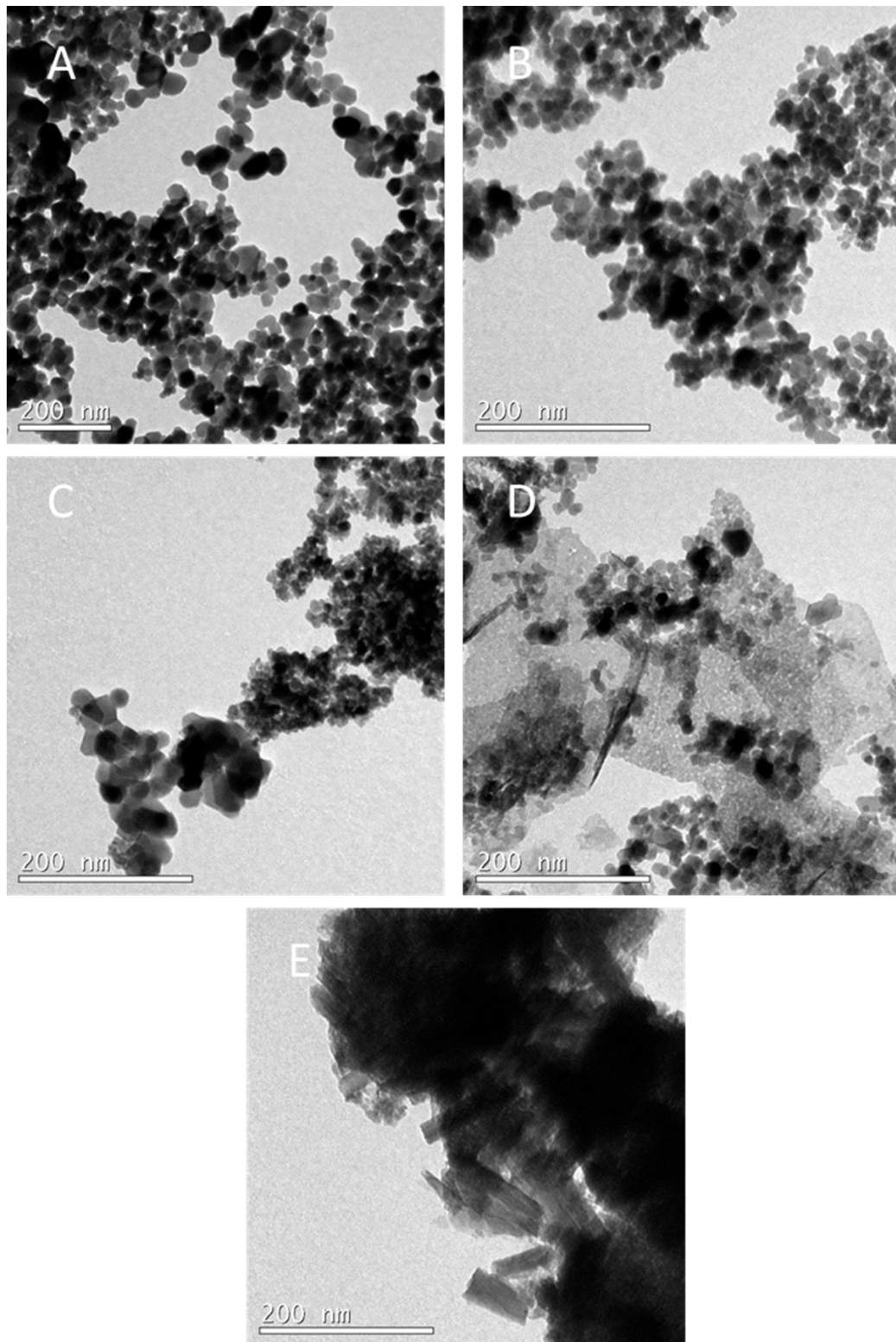


Figure 5. TEM images obtained from the catalyst samples: (A) Co_3O_4 ; (B) $\text{Co}_3\text{O}_4/\text{PVP}$; (C) $\text{Co}_3\text{O}_4/\text{CeO}_2$; (D) $\text{Co}_3\text{O}_4/\text{zeolite}$; (E) $\text{Co}_3\text{O}_4/\text{MnO}_2$.

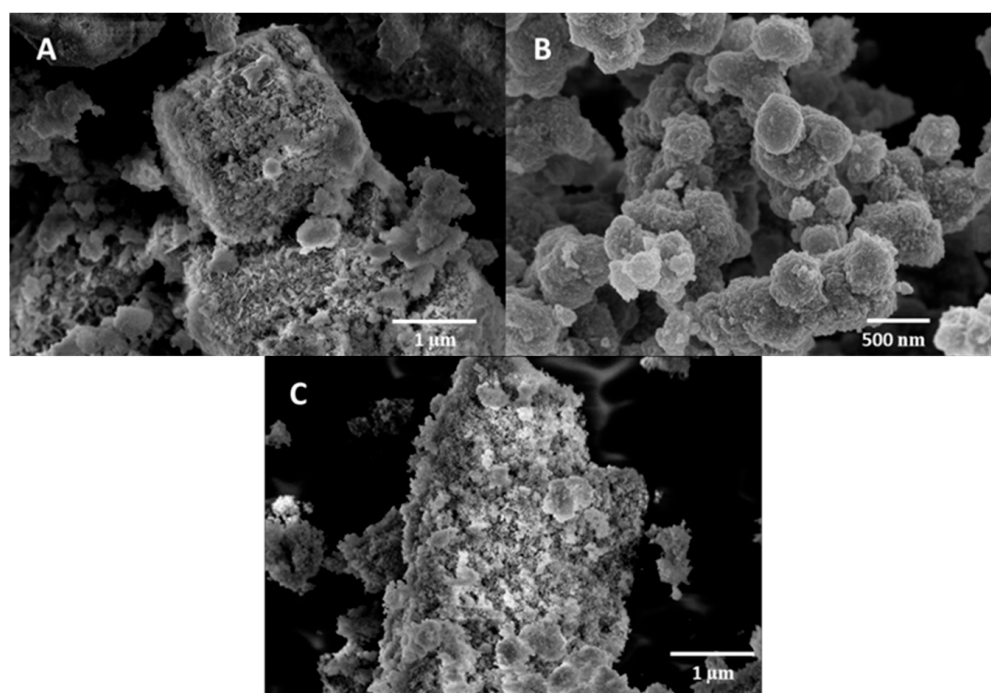


Figure 6. SEM images obtained from the catalyst samples: (A) $\text{Co}_3\text{O}_4/\text{zeolite}$; (B) $\text{Co}_3\text{O}_4/\text{MnO}_2$; (C) $\text{Co}_3\text{O}_4/\text{CeO}_2$.

Co_3O_4 nanoparticles embedded in MnO_2 show an aggregated morphology, as previously reported in the literature (Figure 6B) [25]. This fact is also shown in the TEM image of the same sample (Figure 5E).

The elemental composition of the catalyst samples was determined by energy dispersive spectrometry (EDX). This analysis was carried out on the nanoparticles immobilized on the three tested different supports in order to confirm the presence of the expected elements and possible impurities. The content of the latter is expressed in the “others” row in Tables 1–3 and includes mainly chloride, sodium, and potassium coming from the synthesis process. As observed with XRD, the EDX spectrum of $\text{Co}_3\text{O}_4/\text{zeolite}$ confirms the presence of expected chemical elements (Co, Al, Si) (Table 3) [33]. Nevertheless, a very small presence of impurities from the reducing agent used during the synthesis was also detected, indicating that the material should have been washed more times. Co and Ce were detected in the $\text{Co}_3\text{O}_4/\text{CeO}_2$ sample as expected (Table 2). In the $\text{Co}_3\text{O}_4/\text{MnO}_2$ sample (Table 1), the presence of Co and Mn elements was detected, as well as a very small amount of sodium and potassium.

Table 1. Element quantification with EDX of $\text{Co}_3\text{O}_4/\text{MnO}_2$ material.

Element	Weight (%)	Atomic (%)
C	28.60	43.21
O	38.52	43.68
Mn	14.38	4.75
Co	14.15	4.36
Others	3.81	3.58

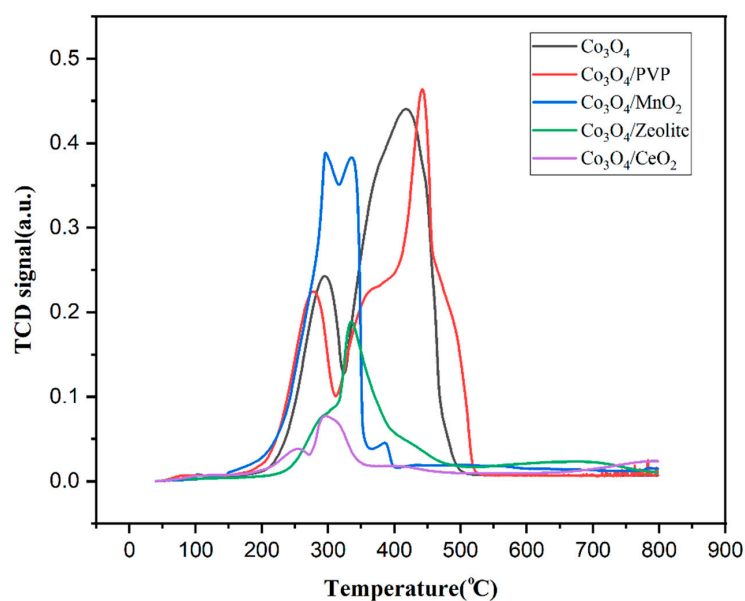
Table 2. Element quantification with EDX of $\text{Co}_3\text{O}_4/\text{CeO}_2$ material.

Element	Weight (%)	Atomic (%)
C	5.44	16.78
O	24.06	55.74
Co	21.43	13.48
Ce	48.46	12.82
Others	0.61	1.18

Table 3. Element quantification with EDX of $\text{Co}_3\text{O}_4/\text{zeolite}$ material.

Element	Weight (%)	Atomic (%)
C	46.01	58.85
O	35.51	34.10
Si	2.12	1.16
Al	2.25	1.28
Co	11.83	3.08
Others	2.28	1.53

The reducibility of the Co_3O_4 catalyst supported on different supports was investigated by hydrogen temperature-programmed reduction (H_2 -TPR) in a 50–800 °C temperature range. The corresponding TPR profiles are shown in Figure 7. As can be observed, a different reduction behavior is obtained for the Co_3O_4 when supported on different materials as a result of the metal–support interaction between Co_3O_4 and the support. The reduction behavior of all samples can be seen to consist of two main peaks. The first peak at lower temperatures (250–300 °C) can be attributed to the well-dispersed Co_3O_4 , while the peaks at higher temperatures (400–500 °C) correspond to the reduction in bulk Co_3O_4 . In general, MnO_2 seems to have had the most constructive effect on the reducibility of Co_3O_4 since the peak corresponding to bulk Co_3O_4 disappeared and the peaks at lower temperatures corresponding to the well-dispersed Co_3O_4 strengthened significantly in the TPR profile of $\text{Co}_3\text{O}_4/\text{MnO}_2$, demonstrating a strong metal–support interaction between Co_3O_4 and MnO_2 , leading to better dispersion of Co_3O_4 nanoparticles. However, this result was not supported by TEM images, as previously discussed.

**Figure 7.** H_2 -TPR profiles of the following samples: Co_3O_4 ; $\text{Co}_3\text{O}_4/\text{PVP}$; $\text{Co}_3\text{O}_4/\text{MnO}_2$; $\text{Co}_3\text{O}_4/\text{zeolite}$; and $\text{Co}_3\text{O}_4/\text{CeO}_2$.

Zeolite can be seen to have also affected the reduction behavior of Co_3O_4 , as there is a broad peak at 250–500 °C for the sample $\text{Co}_3\text{O}_4/\text{zeolite}$, while no peak at higher temperatures can be observed. In addition, CeO_2 support seems to have had a slightly positive effect on the reducibility of Co_3O_4 , as the peak at higher temperatures in the TPR profile of $\text{Co}_3\text{O}_4/\text{CeO}_2$ also disappeared, while two peaks appeared at 250–350 °C. Finally, comparing the profile of Co_3O_4 and $\text{Co}_3\text{O}_4/\text{PVP}$, although there can be seen a slight shift to lower temperatures for the first peak related to dispersed Co_3O_4 and a slight shift to higher temperatures for the peak related to bulk Co_3O_4 , it can be stated that there is no significant change in the reducibility of Co_3O_4 when synthesized using PVP, showing that the metal–support interaction can be considered negligible for the catalyst $\text{Co}_3\text{O}_4/\text{PVP}$.

3.2. Catalytic Activity of the Catalysts

To study the catalytic activity of the samples, methanol STY and selectivity were obtained. Figure 8 presents methanol STY for cobalt and its oxide as a function of operating temperature at pressures of 10 and 15 bar, respectively. The error bars have not been included in the STY figures due to their low values. The effect of the reaction temperature was also investigated, and it can be seen that for cobalt samples methanol STY increases gradually as the temperature rises. However, for the Co_3O_4 catalyst, this increase was not so evident operating at 10 bar, and when the operating pressure was 15 bar, a slight decrease in the STY values as the temperature rises can be detected. On the contrary, in the case of cobalt, the results showed that a better catalytic activity is obtained at 15 bar, which is an expected result, as the use of high pressures is advantageous due to the exothermic nature of the reaction [8,11].

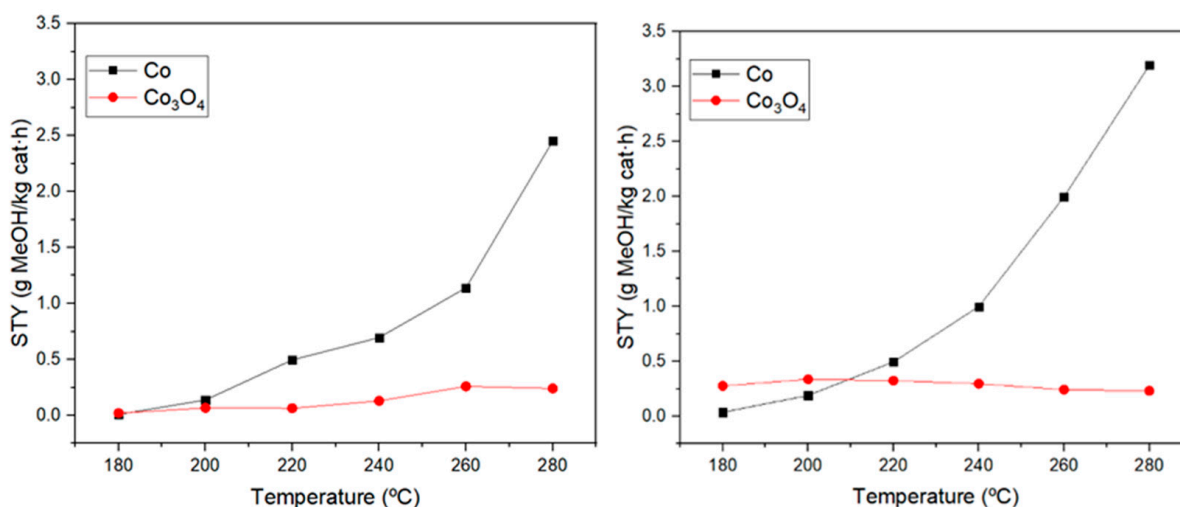


Figure 8. STY values for cobalt and cobalt oxide nanoparticles at a pressure of 10 bar (left) and 15 bar (right).

Furthermore, the catalytic activity of cobalt and cobalt oxide was compared in terms of STY and selectivity to understand which cobalt species presents the active sites more favorable for methanol synthesis. As can be observed in Figure 8, cobalt nanoparticles give a methanol STY of $3.2 \text{ g} \cdot \text{kg}_{\text{catalyst}}^{-1} \text{h}^{-1}$, while only $0.25 \text{ g} \cdot \text{kg}_{\text{catalyst}}^{-1} \text{h}^{-1}$ was obtained for cobalt oxide nanoparticles. Hence, metallic cobalt possesses active sites catalyzing the methanol synthesis from the carbon dioxide hydrogenation reaction more efficiently. This is due to the fact that the selectivity of the reaction is much more favored for methanol formation than for carbon monoxide production when cobalt is used instead of Co_3O_4 because the latter material is highly selective toward methane and carbon monoxide formation [34,35]. In many studies, this effect has been attributed to a lower carbon dioxide adsorption on the cobalt surface compared to Co_3O_4 , which favors the formation

of products, such as methane, when using the oxide [36]. However, the catalyst selected for this study was cobalt oxide due to its high stability compared to elemental cobalt [37].

Two ways to improve the catalytic activity working with cobalt oxide nanoparticles were studied: (a) the addition of polyvinylpyrrolidone (PVP), in order to restrain the overgrowth of the nanoparticles, and (b) the addition of a support, to improve the synergistic effect between the nanoparticles and the support. A comparison of the catalyst's performance with and without PVP was carried out to analyze the effect of this polymer on the materials. The results are shown in Figure 9. By adding PVP in the synthesis of Co_3O_4 , higher methanol STY was obtained, which is accounted for by the smaller size of Co_3O_4 nanoparticles, showing a more spherical morphology (Figure 4C,D). This aspect leads to a higher specific surface area and, therefore, more availability of the catalytic sites.

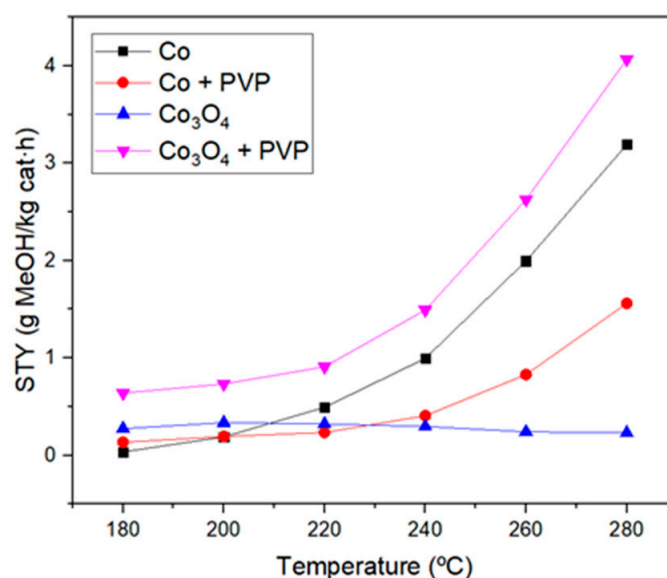


Figure 9. Methanol STY values obtained for cobalt and cobalt oxide nanoparticles with and without PVP at 15 bar.

In order to investigate the impact of supports on the catalytic activity of Co_3O_4 nanoparticles, they were immobilized on different supports including zeolite, CeO_2 , and MnO_2 . As seen in Figure 10, more methanol STY was obtained when immobilizing Co_3O_4 on CeO_2 . This can be attributed to the strong metal–support interaction between Co_3O_4 and CeO_2 , which generates interfacial sites that can synergistically catalyze the methanol synthesis reaction. In addition, oxygen vacancies present in CeO_2 are also assumed to facilitate the adsorption and activation of carbon dioxide [8,20,21,38]. The other support studied was zeolite, which resulted in an improvement of methanol production since the presence of aluminum atoms in these silicate-based materials provides negative charges that are compensated by exchangeable cations in the pore space, and these porous characteristics in the zeolite structure are those that allow greater carbon dioxide adsorption capacity [22,37,39]. Co_3O_4 immobilized on MnO_2 also resulted in more methanol STY compared to Co_3O_4 . This is probably a result of the interactional effect of the two materials, as the catalytic activities of the individual materials are lower and less selective for methanol (Figure 8), indicating the importance of the architecture and nature of the interface [11]. Comparing the methanol STY of the three supports studied, CeO_2 revealed the best results as a support of Co_3O_4 , which can be due to the oxygen vacancies promoting carbon dioxide adsorption and activation, as well as the generation of the interfacial sites between CeO_2 and Co_3O_4 , hence favoring the methanol synthesis reaction. Cobalt oxides have previously been reported to provide a low methanol production yield when compared with supported or modified cobalt compounds. For instance, Wang et al. [12] show that unsupported cobalt oxide shows the lowest yield compared with these species supported on SiO_2 or

modified through linkages with silicon. Li et al. [40] show a similar result when comparing manganese oxide linked supported on cobalt oxide. Although the results make it difficult to compare the catalytic performance of the compounds studied in this work with others in the literature due to the different experimental conditions and material features, it has been previously reported that cobalt oxide species, like In_2O_3 , supported on Co_3O_4 have a catalytic activity that reveals an STY of up to $650 \text{ g}\cdot\text{kg}_{\text{catalyst}}^{-1}\text{h}^{-1}$ [41]. Another similar compound, a cobalt–indium composite obtained by pyrolysis, was evaluated by Wang et al. to perform an STY of $620 \text{ g}\cdot\text{kg}_{\text{catalyst}}^{-1}\text{h}^{-1}$ [42]. However, the compounds studied in the mentioned works are more complex structures, such as a cobalt metal–organic framework impregnated with indium, and a pyrolytic composite of cobalt and indium ($\text{Co}_3\text{InC}_{0.75}\text{-In}_2\text{O}_3$), respectively. Also, the pressures used are much higher; they are 50 bar. Other bimetallic catalysts using noble metals, like palladium, in particular Pd/Zn materials supported on carbon nanotubes, have also obtained high STY values of $371 \text{ g}\cdot\text{kg}_{\text{catalyst}}^{-1}\text{h}^{-1}$ but at higher pressures of 30 bar [43]. The $\text{Co}_3\text{O}_4/\text{CeO}_2$ catalyst analyzed in this study improved the catalytic performance of a material composed of copper and zinc, which are the typical elements used for this catalysis reaction, Cu/ZnO/zeolite, reported by Carrasco García et al. [22]. In particular, the latter obtained an STY of $4.3 \text{ g}\cdot\text{kg}_{\text{catalyst}}^{-1}\text{h}^{-1}$ and $\text{Co}_3\text{O}_4/\text{CeO}_2$ an STY of $8.3 \text{ g}\cdot\text{kg}_{\text{catalyst}}^{-1}\text{h}^{-1}$ at the same temperature and pressure conditions.

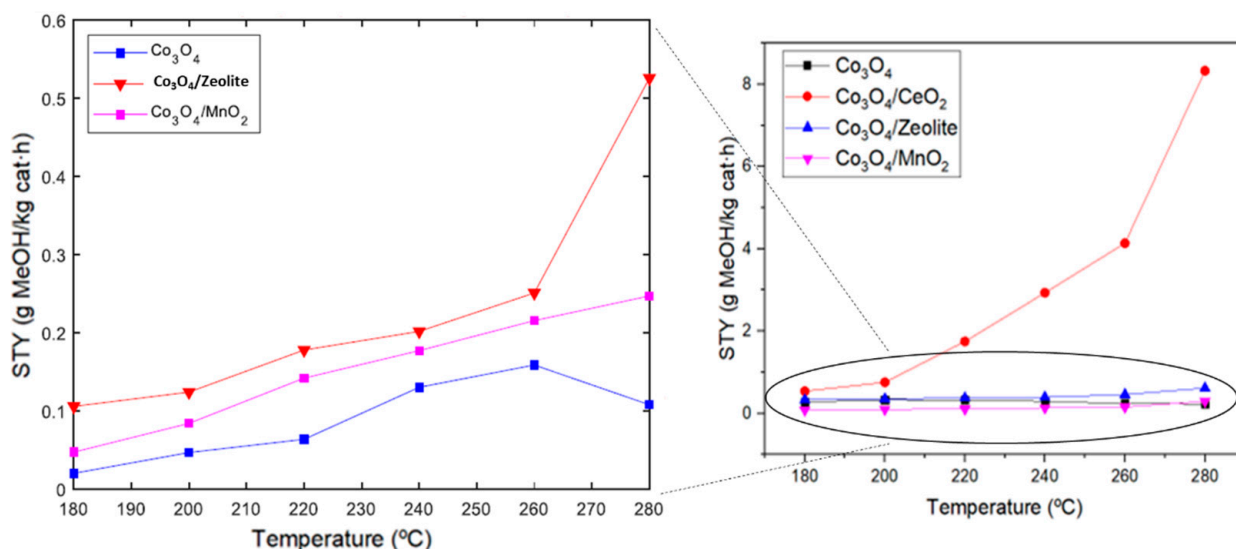


Figure 10. Methanol STY values obtained for samples at different temperatures and a pressure of 15 bar.

Methanol selectivity for the catalyst samples is presented in Figure 11. As can be seen, at 180 °C and 15 bar, the methanol selectivity for all samples was 100%, except for $\text{Co}_3\text{O}_4/\text{CeO}_2$, indicating that no carbon monoxide was formed at this temperature using the indicated materials. Nonetheless, with the temperature increase, methanol selectivity decreases because the change in the enthalpy of methanol synthesis is negative, and, therefore, it is an exothermic reaction, which is more favored at lower temperatures (Figure 11) [9,44]. In the case of Co_3O_4 with PVP and $\text{Co}_3\text{O}_4/\text{zeolite}$, a decrease in selectivity toward methanol was only observed at 220 °C. For the other remaining catalysts, this methanol selectivity decreased considerably because of the production of carbon monoxide at high temperatures (Figure 11) [11,40].

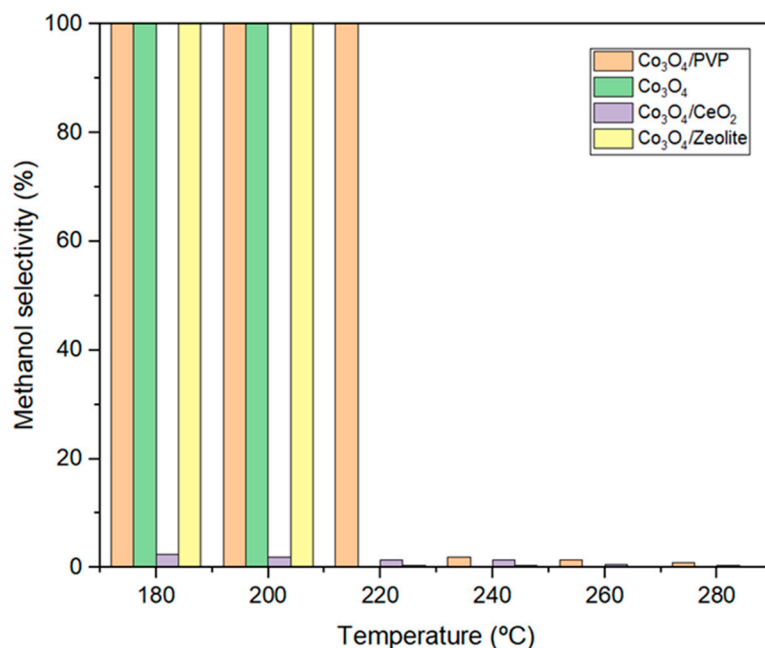


Figure 11. Methanol selectivity (%) values at 15 bar of the best catalysts.

4. Conclusions

In this work, a series of cobalt-based catalysts with different supports were synthesized, and their catalytic activity for methanol production from carbon dioxide hydrogenation was studied. XRD analysis detected the crystalline phase of the samples and confirmed the integration of Co₃O₄ and Co on the supports studied (zeolite, cerium oxide, and manganese oxide). Moreover, it was demonstrated that the addition of PVP as a stabilizing agent improves the catalytic capacity of Co₃O₄, as it helps to obtain more homogeneous and smaller nanoparticles. However, for the Co catalyst synthesized using PVP, this effect was not observed as a result of partial oxidation of the material due to the presence of the stabilizing agent. Comparing the effect of the supports studied, the performance of CeO₂ as support was more promising, which was accounted for by the presence of oxygen vacancies in CeO₂ that promote carbon dioxide adsorption and activation. In addition, the higher catalytic activity of the catalyst supported by CeO₂ can be attributed to the generation of favorable interfacial sites between CeO₂ and Co₃O₄ for the methanol synthesis reaction.

Author Contributions: Conceptualization, A.S. and J.M.-V.; methodology, A.C.-G., Z.B.-A., S.A.V. and A.A.M.; validation, J.M.-V. and A.C.-G.; formal analysis, A.C.-G., J.M.-V., S.A.V. and A.A.M.; investigation, A.C.-G. and J.M.-V.; resources, A.S. and J.M.-V.; data curation, A.C.-G., Z.B.-A. and A.A.M.; writing—original draft preparation, A.C.-G.; writing—review and editing, A.C.-G., J.M.-V., S.A.V., A.A.M. and A.S.; visualization, A.C.-G.; supervision, J.M.-V. and A.S.; project administration, A.S.; funding acquisition, A.S. All authors have read and agreed to the published version of the manuscript.

Funding: This research was funded by Fundación Ramón Areces in the hallmark of the META2NOL project granted in the XIX National Contest of Life and Matter Sciences Projects, grant number CIVP19A5952. This study has been financed by the Spanish Ministerio de Ciencia e Innovación in the call Proyectos de Transición Ecológica y Transición Digital 2022. Squeezer project, ref. TED2021-130407B-I00. Anna Carrasco García thanks UAB for the PIF scholarship granted for the completion of her PhD thesis. Ahmad Abo Markeb thanks the Spanish Ministry of Universities for his Maria Zambrano scholarship, ID 715364.

Institutional Review Board Statement: Not applicable.

Informed Consent Statement: Not applicable.

Data Availability Statement: Data are contained within the article.

Conflicts of Interest: The authors declare no conflicts of interest.

References

1. Masson-Delmotte, V.; Zhai, P.; Pirani, A.; Connors, S.L.; Péan, C.; Berger, S.; Caud, N.; Chen, Y. Climate Change 2021: The Physical Science Basis. In *Contribution of Working Group I to the Sixth Assessment Report of the Intergovernmental Panel on Climate Change*; Cambridge University Press: Cambridge, UK; New York, NY, USA, 2021; p. 3949.
2. Yadav, S.; Mondal, S.S. A review on the progress and prospects of oxy-fuel carbon capture and sequestration (CCS) Technology. *Fuel* **2022**, *308*, 122057. [[CrossRef](#)]
3. Sabri, M.A.; Al Jitan, S.; Bahamon, D.; Vega, L.F.; Palmisano, G. Current and future perspectives on catalytic-based integrated carbon capture and utilization. *Sci. Total Environ.* **2021**, *790*, 148081. [[CrossRef](#)]
4. Song, C. Global challenges and strategies for control, conversion and utilization of CO₂ for sustainable development involving energy, catalysis, adsorption and chemical processing. *Catal. Today* **2006**, *115*, 2–32. [[CrossRef](#)]
5. Olah, G.A. Beyond Oil and Gas: The Methanol Economy. *Angew. Chem. Int. Ed.* **2005**, *44*, 2636–2639. [[CrossRef](#)]
6. Jadhav, S.G.; Vaidya, P.D.; Bhanage, B.M.; Joshi, J.B. Catalytic carbon dioxide hydrogenation to methanol: A review of recent studies. *Chem. Eng. Res. Des.* **2014**, *92*, 2557–2567. [[CrossRef](#)]
7. Li, M.M.J.; Tsang, S.C.E. Bimetallic catalysts for green methanol production via CO₂ and renewable hydrogen: A mini-review and prospects. *Catal. Sci. Technol.* **2018**, *8*, 3450–3464. [[CrossRef](#)]
8. Sha, F.; Han, Z.; Tang, S.; Wang, J.; Li, C. Hydrogenation of Carbon Dioxide to Methanol over Non-Cu-based Heterogeneous Catalysts. *ChemSusChem* **2020**, *13*, 6160–6181. [[CrossRef](#)]
9. Have, I.C.; Kromwijk, J.J.G.; Monai, M.; Ferri, D.; Sterk, E.B.; Meirer, F.; Weckhuysen, B.M. Uncovering the reaction mechanism behind CoO as active phase for CO₂ hydrogenation. *Nat. Commun.* **2022**, *13*, 324. [[CrossRef](#)]
10. Tan, Q.; Shi, Z.; Wu, D. CO₂ Hydrogenation to Methanol over a Highly Active CuNi/CeO₂-Nanotube Catalyst. *Ind. Eng. Chem. Res.* **2018**, *57*, 10148–10158. [[CrossRef](#)]
11. Stangeland, K.; Kalai, D.Y.; Ding, Y.; Yu, Z. Mesoporous manganese-cobalt oxide spinel catalysts for CO₂ hydrogenation to methanol. *J. CO₂ Util.* **2019**, *32*, 146–154. [[CrossRef](#)]
12. Wang, L.; Guan, E.; Wang, Y.; Wang, L.; Gong, Z.; Cui, Y.; Meng, X.; Gates, B.C.; Xiao, F.S. Silica accelerates the selective hydrogenation of CO₂ to methanol on cobalt catalysts. *Nat. Commun.* **2020**, *11*, 1033. [[CrossRef](#)]
13. Zhou, Y.; Jiang, Y.; Qin, Z.; Xie, Q.; Ji, H. Influence of Zr, Ce, and La on Co₃O₄ catalyst for CO₂ methanation at low temperature. *Chin. J. Chem. Eng.* **2018**, *26*, 768–774. [[CrossRef](#)]
14. Suslova, E.V.; Chernyak, S.A.; Egorov, A.V.; Savilov, S.V.; Lunin, V.V. CO₂ hydrogenation over cobalt-containing catalysts. *Kinet. Catal.* **2015**, *56*, 646–654. [[CrossRef](#)]
15. Wang, L.; Wang, L.; Zhang, J.; Liu, X.; Wang, H.; Zhng, W.; Yang, Q.; Ma, J.; Dong, X.; Jo Yoo, S.; et al. Selective Hydrogenation of CO₂ to Ethanol over Cobalt Catalysts. *Angew. Chem. Int. Ed.* **2018**, *57*, 6104–6108. [[CrossRef](#)]
16. Ouyang, B.; Xiong, S.; Zhang, Y.; Liu, B.; Li, J. The study of morphology effect of Pt/Co₃O₄ catalysts for higher alcohol synthesis from CO₂ hydrogenation. *Appl. Catal. A Gen.* **2017**, *543*, 189–195. [[CrossRef](#)]
17. Tursunov, O.; Tilyabaev, Z. Hydrogenation of CO₂ over Co supported on carbon nanotube, carbon nanotube-Nb₂O₅, carbon nanofiber, low-layered graphite fragments and Nb₂O₅. *J. Energy Inst.* **2019**, *92*, 18–26. [[CrossRef](#)]
18. Fan, T.; Liu, H.; Shao, S.; Gong, Y.; Li, G.; Tang, Z. Cobalt Catalysts Enable Selective Hydrogenation of CO₂ toward Diverse Products: Recent Progress and Perspective. *J. Phys. Chem. Lett.* **2021**, *12*, 10486–10496. [[CrossRef](#)]
19. Pérez-Botella, E.; Valencia, S.; Rey, F. Zeolites in Adsorption Processes: State of the Art and Future Prospects. *Chem. Rev.* **2022**, *122*, 17647–17695. [[CrossRef](#)]
20. Dou, J.; Tang, Y.; Nie, L.; Andolina, C.M.; Zhang, X.; House, S.; Li, Y.; Yang, J.; Tao, F. Complete Oxidation of Methane on Co₃O₄/CeO₂ Nanocomposite: A Synergic Effect. *Catal. Today* **2018**, *311*, 48–55. [[CrossRef](#)]
21. Liu, X.; Zhou, K.; Wang, L.; Wang, B.; Li, Y. Oxygen vacancy clusters promoting reducibility and activity of ceria nanorods. *J. Am. Chem. Soc.* **2009**, *131*, 3140–3141. [[CrossRef](#)]
22. Carrasco Garcia, A.; Moral-Vico, J.; Markeb, A.A.; Sanchez, A. Conversion of Carbon Dioxide into Methanol Using Cu-Zn Nanostructured Materials as Catalysts. *Nanomaterials* **2022**, *12*, 999. [[CrossRef](#)]
23. Javed, R.; Zia, M.; Naz, S.; Aisida, S.O.; ul Ain, N.; Ao, Q. Role of capping agents in the application of nanoparticles in biomedicine and environmental remediation: Recent trends and future prospects. *J. Nanobiotechnology* **2020**, *18*, 172. [[CrossRef](#)] [[PubMed](#)]
24. Zhao, Y.W.; Zheng, R.K.; Zhang, X.X.; Xiao, J.Q. A simple method to prepare uniform Co nanoparticles. *IEEE Trans. Magn.* **2003**, *39*, 2764–2766. [[CrossRef](#)]
25. Worku, A.K.; Ayele, D.W.; Habtu, N.G.; Yemata, T.A. Engineering Co₃O₄/MnO₂ nanocomposite materials for oxygen reduction electrocatalysis. *Heliyon* **2021**, *7*, e08076. [[CrossRef](#)]
26. Natile, M.M.; Glisenti, A. CoO_x/CeO₂ Nanocomposite Powders: Synthesis, Characterization, and Reactivity. *Chem. Mater.* **2005**, *17*, 3403–3414. [[CrossRef](#)]
27. Jincy, C.S.; Meena, P. Synthesis of Co₃O₄ nanoparticles for sensing toxic gas at room temperature. *Mater. Today Proc.* **2020**, *33*, 2362–2365. [[CrossRef](#)]

28. Zamani, F.; Rezapour, M.; Kianpour, S. Immobilization of L-Lysine on Zeolite 4A as an Organic-Inorganic Composite Basic Catalyst for Synthesis of α,β -Unsaturated Carbonyl Compounds under Mild Conditions. *Bull. Korean Chem. Soc.* **2013**, *34*, 2367–2374. [[CrossRef](#)]
29. Wang, C.; Zhang, C.; Hua, W.C.; Guo, Y.; Lu, G.Z.; Gil, S.; Giroir-Fendler, A. Catalytic oxidation of vinyl chloride emissions over Co-Ce composite oxide catalysts. *Chem. Eng. J.* **2017**, *315*, 392–402. [[CrossRef](#)]
30. Palacio, R.; Torres, S.; Lopez, D.; Hernandez, D. Selective glycerol conversion to lactic acid on $\text{Co}_3\text{O}_4/\text{CeO}_2$ catalysts. *Catal. Today* **2018**, *302*, 196–202. [[CrossRef](#)]
31. Feng, L.; Xuan, Z.; Zhao, H.; Bai, Y.; Guo, J.; Su, C.; Chen, X. MnO_2 prepared by hydrothermal method and electrochemical performance as anode for lithium-ion battery. *Nanoscale. Res. Lett.* **2014**, *9*, 290. [[CrossRef](#)]
32. Feng, M.; Zhang, G.; Du, Q.; Su, L.; Ma, Z.; Qin, X.; Shao, G. $\text{Co}_3\text{O}_4@\text{MnO}_2$ core shell arrays on nickel foam with excellent electrochemical performance for aqueous asymmetric supercapacitor. *Ionics* **2017**, *23*, 1637–1643. [[CrossRef](#)]
33. Davar, F.; Fereshteh, Z.; Shoja Razavi, H.; Razavi, R.S.; Loghman-Estarki, M.R. Synthesis and characterization of cobalt oxide nanocomposite based on the Co_3O_4 -zeolite Y. *Superlattices Microstruct.* **2014**, *66*, 85–95. [[CrossRef](#)]
34. Gupta, S.; Ciotonea, C.; Royer, S.; Daquin, J.; Vinod, C.P. Engineering pore morphology using silica template route over mesoporous cobalt oxide and its implications in atmospheric pressure carbon dioxide hydrogenation to olefins. *Appl. Mater. Today* **2020**, *19*, 100586. [[CrossRef](#)]
35. Jampaiah, D.; Damma, D.; Chalkidis, A.; Venkataswamy, P.; Bhargava, S.K.; Reddy, B.M. MOF-derived ceria-zirconia supported Co_3O_4 catalysts with enhanced activity in CO_2 methanation. *Catal. Today* **2020**, *356*, 519–526. [[CrossRef](#)]
36. Díez-Ramírez, J.; Sanchez, P.; Kyriakou, V.; Zafeiratos, S.; Marnellos, G.E.; Konsolakis, M.; Dorado, F. Effect of support nature on the cobalt-catalyzed CO_2 hydrogenation. *J. CO₂ Util.* **2017**, *21*, 562–571. [[CrossRef](#)]
37. Gabe, A.; García-Aguilar, J.; Berenguer-Murcia, A.; Morallón, E.; Cazorla-Amorós, D. Key factors improving oxygen reduction reaction activity in cobalt nanoparticles modified carbon nanotubes. *Appl. Catal. B Environ.* **2017**, *217*, 303–312. [[CrossRef](#)]
38. Jiang, F.; Wang, S.; Liu, B.; Liu, J.; Wang, L.; Xiao, Y.; Xu, Y.; Liu, X. Insights into the Influence of CeO_2 Crystal Facet on CO_2 Hydrogenation to Methanol over Pd/ CeO_2 Catalysts. *ACS Catal.* **2020**, *10*, 11493–11509. [[CrossRef](#)]
39. Choi, S.; Drese, J.H.; Jones, C.W. Adsorbent materials for carbon dioxide capture from large anthropogenic point sources. *ChemSusChem* **2009**, *2*, 796–854. [[CrossRef](#)] [[PubMed](#)]
40. Li, C.S.; Melaet, G.; Ralston, W.T.; An, K.; Brooks, C.; Ye, Y.; Liu, Y.S.; Zhu, J.; Guo, J.; Alayoglu, S.; et al. High-performance hybrid oxide catalyst of manganese and cobalt for low-pressure methanol synthesis. *Nat. Commun.* **2015**, *6*, 6538. [[CrossRef](#)]
41. Pustovarenko, A.; Dikhtiarenko, A.; Bavykina, A.; Gevers, L.; Ramírez, A.; Russkikh, A.; Telalovic, S.; Aguilar, A.; Hazemann, J.L.; Ould-Chikh, S.; et al. Metal–Organic Framework-derived synthesis of cobalt indium catalysts for the hydrogenation of CO_2 to methanol. *ACS Catal.* **2020**, *10*, 5064–5076. [[CrossRef](#)]
42. Wang, Y.; Yang, B.; Gao, B.; Li, L.; Zhou, Y.; Zhang, Y.; Ishihara, T.; Guo, L. $\text{Co}_3\text{InC}_{0.75}\text{-In}_2\text{O}_3$ composite construction and its synergetic hydrogenation catalysis of CO_2 to methanol. *Appl. Catal. A General* **2023**, *665*, 119374. [[CrossRef](#)]
43. Liang, X.; Dong, X.; Lin, G.; Zhang, H. Carbon nanotube-supported Pd–ZnO catalyst for hydrogenation of CO_2 to methanol. *Appl. Catal. B Environ.* **2009**, *88*, 315–322. [[CrossRef](#)]
44. Ronda-Lloret, M.; Wang, Y.; Oulego, P.; Rothenberg, G.; Tu, X.; Shiju, N.R. CO_2 Hydrogenation at Atmospheric Pressure and Low Temperature Using Plasma Enhanced Catalysis over Supported Cobalt Oxide Catalysts. *ACS Sustain. Chem. Eng.* **2020**, *8*, 17397–17407. [[CrossRef](#)] [[PubMed](#)]

Disclaimer/Publisher’s Note: The statements, opinions and data contained in all publications are solely those of the individual author(s) and contributor(s) and not of MDPI and/or the editor(s). MDPI and/or the editor(s) disclaim responsibility for any injury to people or property resulting from any ideas, methods, instructions or products referred to in the content.